Evaluation Report on Deep-Sky Imaging Performance

of the OCAL H-2 Refractor Astrograph

Sponsors: OCAL, GEMINI, CLEARSKY

Evaluator: Yookov Franklin Zhu

Evaluation Site: Clearsky Desert Observatory — Remote Astronomical Station (Yiwen Station)

Evaluation Period: March 20 – May 5, 2026

1. Abstract

This is my first evaluation of professional deep-sky imaging equipment. We extend our sincere gratitude to OCAL, Clearsky, and Gemini for their generous support of this evaluation.

The evaluation system was paired with a monochrome cooled CMOS camera (QHY268M) and operated remotely at the Yiwen station. Test targets included a high-resolution structured galaxy (M51) and a low-contrast dark nebula (LDN 1320), with total exposure time exceeding 25 hours per target.

The evaluation focused on the following core performance metrics:

- (1) Limiting resolving power of the optical system (stellar FWHM and structural resolution);
- (2) Wide-field uniformity and star-image quality at the field edge;
- (3) SNR performance and background modeling capability for low-surface-brightness structures;
- (4) Long-integration stability and calibration repeatability of the system.

Results indicate that under typical 2″–3″ atmospheric seeing conditions, the measured stellar FWHM reached 2.8525″, and the mean FWHM across the stacked field was approximately 5.78″, approaching the theoretical sampling limit. For the low-contrast dark nebula, after a cumulative integration of over 26.5 hours, the background RMS was controlled to 5.2 ADU, and dust structures with surface brightness below 28.3 mag/arcsec^2 were successfully recorded. The M51 dataset accumulated approximately 41.24 hours of total integration, yielding a spiral arm SNR of 3.8; the tidal bridge's low-surface-brightness structure was clearly discernible, verifying the long-term stability of both the optical system and the tracking platform.

Overall assessment indicates that, even in a high-speed wide-field configuration, the system maintains excellent point-spread-function (PSF) control and high SNR efficiency, placing it in the high-performance tier among amateur-grade instruments. It demonstrates strong all-round capability for imaging faint structures and recording high-resolution galaxy detail, establishing a sound technical foundation for future deep sky surveys or long-term monitoring of specific targets.

2. H-2 Basic Specifications

Focal Length	Focal Ratio	Secondary Minor Axis	Good-Image Circle	Primary/Secondary Material	Weight	Corrector
560 mm	F/2.72	80 mm	44 mm (Full Frame)	Fused Silica Glass	12.7 kg	4-element apochromatic corrector

2.1 Additional Equipment

Parameter	QHY268M	QHY5III200M

Sensor	SONY IMX571	SC2210
Color Version	Monochrome	Monochrome
Sensor Size	APS-C	1/1.8"
Pixel Size	3.76 μm × 3.76 μm	4 μm × 4 μm
Effective Resolution	6252 × 4176	1920 × 1080
Full Resolution	6280 × 4210 (incl. optical black & overscan)	—
Effective Pixels	26 MP	2 MP
Full Well Capacity	Standard: 51 ke$^-$; Extended: 80 ke$^-$	8 ke$^-$
ADC Depth	Native 16-bit (0–65535 DN)	12-bit (output 8 or 16-bit)
Read Noise	1.1–3.5 e$^-$ (photo mode); 2.7–5.5 e$^-$ (extended full-well)	0.75–3 e$^-$ (Gain 0–500)
Dark Current	0.0005 e$^-$ /px/s @ −20 °C; 0.001 e$^-$ /px/s @ −10 °C	—
Exposure Range	0.3 μs – 3600 s	15 μs – 900 s
Amp Glow	Zero amp glow	—
Shutter	Electronic rolling shutter	Electronic rolling shutter
Cooling	Dual-stage TEC	None
Optical Window	AR+AR dual-side anti-reflection coating	AR glass (IR850 filter included)
Back Focus	14.5 mm (±0.3 mm)	8 ± 0.5 mm

2.2 Equatorial Mount: Clearsky ST20

Parameter	Specification
Drive System	High-precision harmonic drive + timing belt
Materials	Anodized 6061 aluminum, 304 stainless steel, brass
RA Axis	42 stepper motor, 20-type harmonic drive, 300:1 reduction ratio
Dec Axis	42 stepper motor, 17-type harmonic drive, 300:1 reduction ratio
Payload Capacity	20–30 kg
GOTO Slew Speed	2°/s (max 6°/s)
Electronic Polar Scope	iPolar / PoleMaster
Power-off Brake	RA electronic brake, ≥68 N·m
Home Position	Electronic home / optional mechanical home

Limit Stops	Standard patented mechanical limit stops
Communication	USB, Bluetooth, Wi-Fi, ST4
Controller Firmware	ONSTEP / ONSTEPX

2.3 Observing Site Conditions

- Location: Minqin County, Wuwei City, Gansu Province
- Observatory: Clearsky Desert Observatory — Remote Astronomical Station
- Coordinates: 38.90° N, 103.38° E
- Bortle Sky Class: Class 1

3. Imaging Strategy and Data Acquisition

3.1 Target Selection

① M51 — Resolution and Structural Resolution Verification

Rationale:

- Spiral arms contain abundant Hα emission regions
- Features tidal bridges and slender dust lanes
- Rich structural scales from arcminute-level to arcsecond-level

Technical Significance:

- Probing the FWHM lower limit under good seeing conditions
- Assessing PSF consistency between the nuclear region and the outer disk
- Verifying field flatness of the fast F/2.72 system

Observational Advantages:

- Declination +47°, near the zenith
- Long observable window during spring nights
- High structural detail density for revealing the optic's limiting performance

② LDN 1320 — Low-Contrast and Dynamic-Range Limit Verification

Rationale:

- Extremely low surface brightness dark nebula
- Gradual, faint background dust extinction
- Highly sensitive to flat-field calibration and background modeling

Technical Significance:

- Testing background noise control capability
- Verifying whether the optical system exhibits residual vignetting
- Measuring SNR improvement efficiency under long-duration integration

Observational Advantages:

- Near the north celestial pole — observable all night
- Low tolerance for image-processing errors
- Validates capability for imaging faint low-contrast structures

In summary, target selection was driven not by visual appeal but by the aim of probing the system's performance boundaries. By combining targets of different scales, contrasts, and physical characteristics, a comprehensive characterization of the H-2's true imaging performance envelope can be achieved under real observing conditions.

3.2 Exposure Structure

LDN 1320:

Channel	Single-Frame Exposure	Total Duration (hours)
L	300 s	10
R	300 s	5.5
G	300 s	5.5
B	300 s	5.5

M51:

Channel	Single-Frame Exposure	Total Duration (hours)
L	300 s	20
R	300 s	7.08
G	300 s	7.08
B	300 s	7.08

4. Imaging Calibration

4.1 Optical Collimation

Short-focal-ratio telescopes (typically defined as f/4 or faster, such as the OCAL H-2 at F/2.72) are inherently far more challenging to collimate than medium-to-long focal-ratio instruments (f/5 or longer). Their optical design means that even a minute collimation error is rapidly amplified by the optical system, directly causing star-image distortion, field non-uniformity, and resolution degradation. The following analysis systematically examines the collimation challenges across four dimensions: optical principles, mechanical design, calibration procedure, and environmental interference.

(1) Optical Principles: Inherent Low Tolerance to Collimation Error

The fundamental requirement of collimation is that the optical axes of the primary mirror, secondary mirror, focuser, and camera sensor plane must all be rigorously co-linear. The optical design of short-focal-ratio telescopes makes this co-linearity requirement extremely unforgiving, manifesting in three key characteristics:

1. Significant Angular Amplification of Collimation Offset

With a short focal length and wide field, even a tiny linear offset of the secondary mirror (e.g., 0.1 mm) produces a far larger angular deviation at the focal plane than it would in a long-focus instrument. The angular deviation $\theta = \arctan(\Delta d / f)$, so the shorter f, the larger θ for the same linear offset:

- Example: F/2.72, 560 mm focal length — a 0.1 mm secondary offset ≈ 0.0103° (37.08″);
- Comparison: F/8, 2000 mm focal length — same 0.1 mm offset ≈ 0.00286° (10.3″).

Deep-sky imaging with a fast telescope typically requires the collimation angular error to be ≤5″, otherwise stars show obvious elongation and trailing. This means the allowable linear tolerance must be held within 0.013 mm — a precision requirement several times more demanding than for a long-focus instrument.

2. Exponentially Higher Aberration Sensitivity

To achieve a wide field and fast focal ratio, fast telescopes incorporate more optical elements (e.g., the 4-element apochromatic corrector in the OCAL H-2), and the primary mirror is typically a paraboloid or hyperboloid — both of which are highly intolerant of collimation error:

- Combined coma and astigmatism: Even a slight axial misalignment simultaneously produces coma and astigmatism at the wide-field edge. These two aberrations compound each other, appearing as star images that are both trailed and deformed — far more difficult to correct through collimation than the single aberrations seen in long-focus instruments.
- Amplified field curvature and distortion: Axial non-co-linearity exacerbates the inherent field curvature of fast optics, causing simultaneous defocus of stars at both the center and edge of the field. The distortion pattern also shifts from regular barrel/pincushion to irregular — further complicating collimation.

3. Narrow Effective Collimation Zone at the Focal Plane

Fast telescopes have an extremely shallow depth of focus ($\Delta f = 2\lambda F^2$). For F/2.72 at 550 nm, depth of focus ≈ $2 \times 550 \times 10^{-6} \times 7.3984 \approx 0.0081$ mm, far shallower than the 0.0704 mm depth of focus of an F/8 instrument. This means that even a 0.01 mm loosening of the focuser during the calibration process can shift the focal plane away from the co-linear axis position, resulting in the collimation destabilizing the moment the focus is slightly adjusted.

(2) Mechanical Design: Structural Constraints That Complicate Collimation

1. Limited Adjustment Space for the Secondary Mirror

The short tube and large aperture-to-focal-length ratio of fast telescopes mean the secondary mirror is mounted on a small bracket at the front of the tube. The multi-vane spider design (typically 3 or 4 vanes to minimize diffraction) leaves little room for adjustment:

- The centration adjustment (lateral shift) has very short travel (≤0.5 mm), so a slight turn of the adjusting screw can easily exceed the allowable linear tolerance — making it easy to mis-adjust and difficult to achieve precise alignment;

- The tilt adjustment (angular) is difficult to control precisely. At F/2.72, a 0.01° tilt error in the secondary mirror produces >10″ of focal-plane axis deviation, while conventional tools (e.g., hex keys) cannot achieve micron-level tilt adjustment.

2. Compounded Co-axiality Requirements with Multiple Optical Elements

Fast telescopes incorporate multiple correctors, filters, and field-flatteners to correct inherent aberrations (e.g., the 4-element corrector in the OCAL H-2). Each additional element adds its own co-axiality requirement:

- Mounting misalignment of the corrector cell, non-uniform filter thickness, and field-flattener tilt angle each become independent sources of collimation error that ultimately add together;
- These elements are typically internal and cannot be removed for individual calibration; only global axis adjustment is possible, making it difficult to isolate individual error sources and achieve precise overall alignment.

3. Lightweight Construction Prone to Post-Collimation Drift

- The tube flexes slightly under temperature change, transport vibration, and gravitational deflection, causing a calibrated axis to ‘drift back’;
- Connection points such as M42 threads and dovetail slots have limited clamping force in lightweight designs, so slight loosening can develop during long imaging sessions, further worsening collimation;
- Payload imbalance on the equatorial mount (e.g., a weight-shifted camera) imparts a small tube tilt that indirectly introduces collimation error.

4. No Standardized Datum for Camera Sensor Tilt Alignment

- With no locating pin between the focuser and camera, a rotational error upon camera installation (e.g., 1° rotation) shifts the sensor center off the optical axis, which at short focal ratios manifests as star-image distortion at the field edges;
- Without a dedicated sensor-leveling tool, alignment is judged by eye or from star images, falling far short of the required precision (≤0.05° sensor tilt tolerance).

(3) Calibration Procedure: Complex Process with Ambiguous Criteria

1. Multi-Step Iterative Collimation Procedure

A complete optical collimation of a fast telescope follows a ‘coarse → fine → verify → re-check’ iterative loop:

1. Coarse collimation: Adjust the three primary-mirror cell screws to correct cone error, bringing the axial angular deviation to ≤1°;
2. Secondary fine collimation: Adjust secondary centration and tilt until the on-axis star image is a perfect circle with no elongation;
3. Focuser / camera alignment: Adjust focuser concentricity and sensor tilt until edge stars match the center star profile;
4. Field verification: Capture a wide-field star image and inspect roundness and FWHM across the entire field; re-collimate if edge stars show distortion;

5.Environmental re-verification: Re-check after temperature change and gravitational flexure to ensure stable collimation.

A long-focus instrument typically requires only secondary centration plus central star verification — roughly half the procedural complexity.

2. Ambiguous Calibration Criteria — Star-Test Reliability Greatly Reduced

- At the wide-field scale of a fast telescope, the apparent size of a star image is small (only 3–5 pixels in the focal plane at 560 mm focal length), so minor collimation errors causing elongation or tailing are difficult to discern visually or with standard software;
- The extremely shallow depth of focus means a slightly defocused star is easily confused with a collimation error, potentially causing the calibrator to adjust focus when they should be adjusting collimation, leading to incorrect corrections;
- Low-surface-brightness background noise masks faint-star detail, while saturated bright stars distort star-image shapes, making it difficult to identify the ‘ideal star’ needed as a calibration reference.

3. High Demands on Calibration Tools and Software

- Hardware tools: Micrometer-precision secondary adjusters, sensor-tilt gauges, laser collimators (accuracy ≤0.01 mm), and angle gauges are required. These are expensive and demand specialist operating skills;
- Software tools: PixInsight PSF fitting is needed to analyze roundness, FWHM, and centroid positions quantitatively rather than relying on visual judgment, imposing high software proficiency requirements on the operator;
- No integrated calibration tool exists; all tools are used independently, requiring manual aggregation of measurements from multiple instruments, which increases procedural error and complexity.

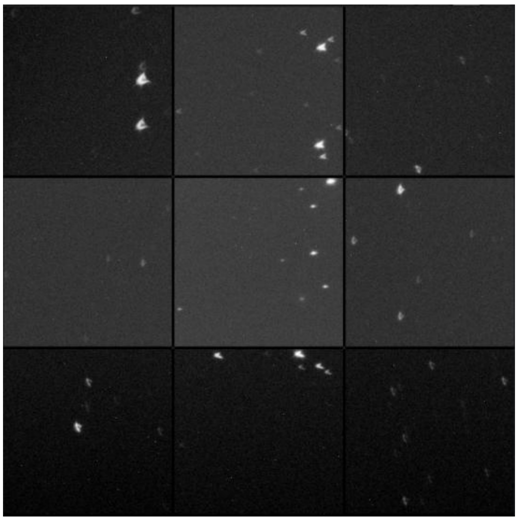

[Figure 4-1: Uncollimated star images]

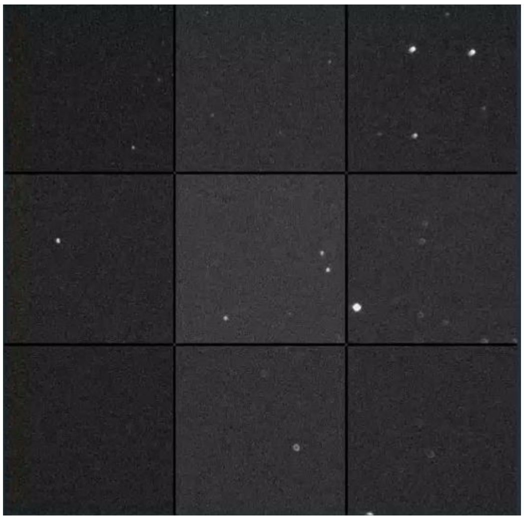

[Figure 4-2: Post-collimation star images]

(Comparison images from a 5-minute exposure of M44 (NGC 2632) used for aberration verification during the evaluation.)

(4) Core Summary: Fast-Telescope Collimation Challenges

The difficulties of collimating a fast telescope are fundamentally the product of ‘inherently low optical tolerance’ combined with ‘high sensitivity of the mechanical design, operating procedure, and environment.’ The core contradiction is: precision requirements are extremely high, but operability, criterion clarity, and precision retention are all extremely low.

Every challenge ultimately converges on a single result: a tiny error is amplified by the fast focal ratio into a large degradation of image quality — manifesting as star-image distortion, field non-uniformity, reduced resolution, and lower SNR on low-surface-brightness targets. This is the fundamental reason why fast telescopes, despite their advantages of wide field and fast exposure, present a steep operational barrier for amateur astronomers.

Furthermore, fast-telescope collimation is not a single-step problem but a systemic one encompassing optics, mechanics, procedure, and environment. Achieving and maintaining precise collimation requires a comprehensive solution: optimized optical design + upgraded mechanical construction + dedicated tooling + standardized operating procedures + environmental adaptation strategies. No single element can be omitted.

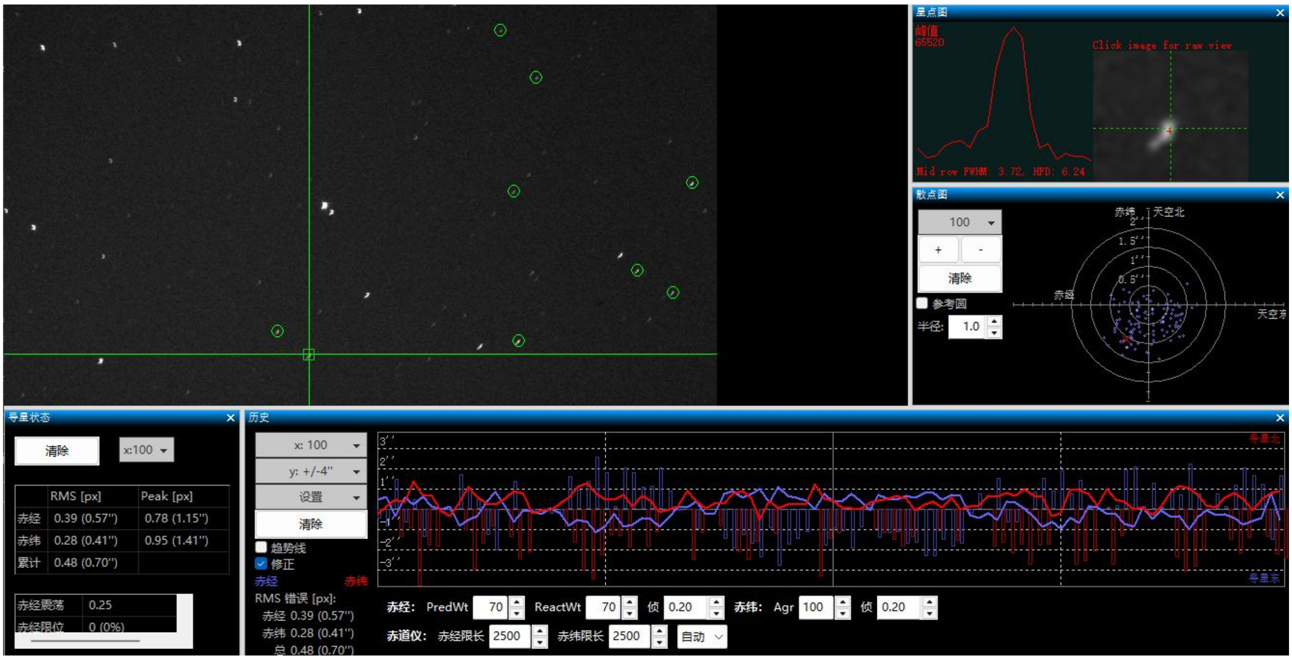

Figure 4-3: Guiding performance during pre-session collimation

4.2 Guiding Error Analysis

The Clearsky ST20 harmonic-drive equatorial mount, when paired with an OAG (Off-Axis Guider), exhibited a phenomenon of sudden guiding error spikes followed by rapid recovery. The cause is likely concentrated in four areas: OAG optical-path transient interference, guiding camera momentary anomalies, mount dynamic-load / environmental disturbances, and guiding software parameter mismatch. The ‘sudden spike, rapid recovery’ signature points to transient, non-persistent external or incidental factors rather than damage to the mechanical structure or core components.

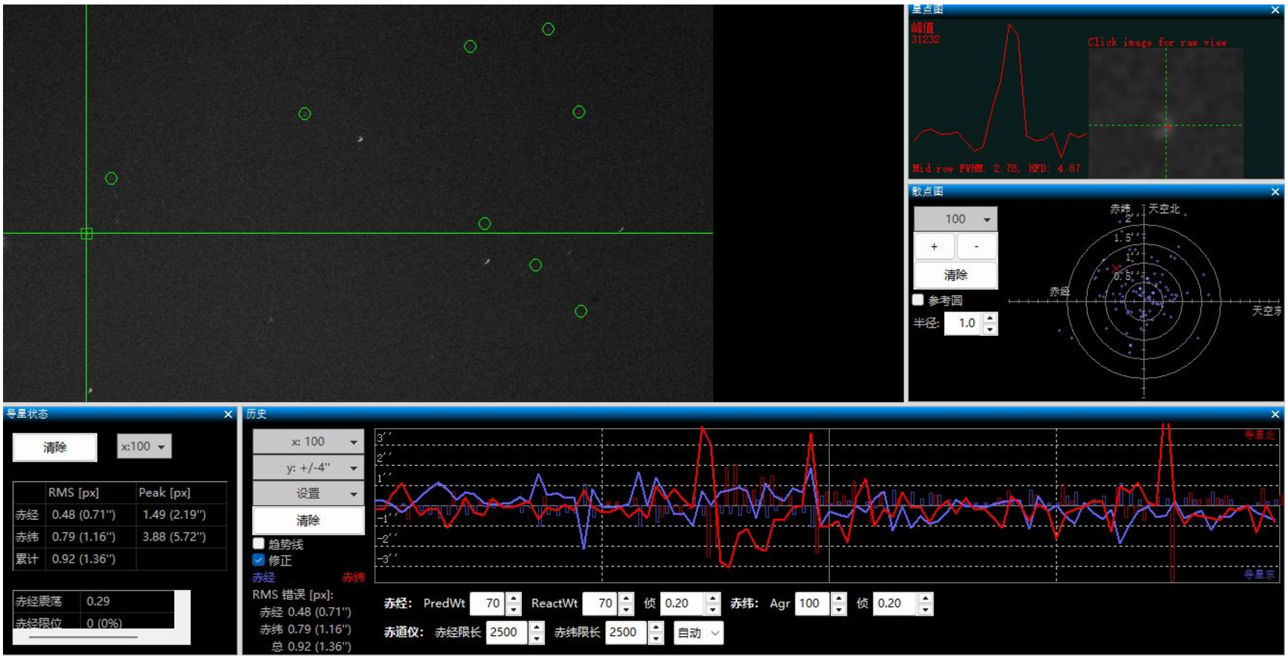

Figure 4-4: Data showing instantaneous guiding error spikes

I. Transient OAG Optical-Path Obstruction / Defocus

The OAG extracts a guiding beam via an off-axis prism in the main optical path. Its lack of independent focus, complete coupling to the main optical path, and high susceptibility of the prism to mechanical micro-vibration make it the primary cause of sudden guiding errors. Because optical-path interference is typically 'instantaneous and fleeting,' it closely matches the observed fault signature:

1. Instantaneous Micro-Tilt / Shift of the OAG Prism from Mechanical Vibration

- During mount acceleration/deceleration, meridian flip, or target altitude changes, inertial forces are transmitted to the OAG, causing the prism to momentarily tilt (<0.05°) or shift axially. The guiding beam deflects instantaneously, the guide star image shows trailing and elongation, and the guiding software reports a sharp error spike;
- Once the mount settles into stable tracking and inertial forces subside, the prism returns to its nominal position under mechanical spring tension, the optical path normalizes, and the error rapidly falls back.

2. Transient Dust / Condensation Obscuring the Guider Aperture

- When airflow or tube vibration moves a dust particle, the guide star is momentarily partially obscured (brightness drops / shape distorts), causing the guiding software to lose accurate centroid fit and report a large error;
- Once the particle is blown clear or moisture briefly evaporates, the guide star is fully recovered and the software re-acquires a precise lock.

3. Instantaneous Co-Focus Shift of the Primary Mirror

- When atmospheric seeing momentarily degrades or tube temperature changes slightly, the primary focal point drifts by a few microns, the guiding path defocuses simultaneously, the guide-star centroid fit degrades, and the error spikes;
- When seeing recovers and the tube temperature stabilizes, the focal point returns and the error quickly falls back.

4. Transient Play in the OAG-Camera Flange Connection

If the flange locking screws are not fully tightened, tracking micro-vibration causes momentary relative motion between the OAG and the main camera. The guide-star position shifts instantaneously, software reports increased error; the moment the play disappears, the error recovers immediately.

II. Transient Hardware / Signal Anomalies of the Guide Camera (QHY5III200M)

1. Instantaneous Supply-Voltage Fluctuation

- A transient voltage drop (e.g., 5 V → 4.5 V) disturbs the readout circuit, causing noise spikes and centroid shifts in the guide-star data, driving the error value sharply upward;
- Once the power contact stabilizes and ripple disappears, the camera resumes normal acquisition and the error immediately drops.

2. Transient Data Packet Loss / Latency

- USB / Bluetooth transmission interference (e.g., from the mount motor or cooled camera EMI) causes momentary packet loss; the software receives an incomplete or delayed star image, centroid fit degrades, and error spikes;
- Once the interference clears and transmission normalizes, the error rapidly recovers.

3. Transient Cosmic-Ray / Thermal Noise Hit

- A cosmic-ray event on the sensor generates a bright transient pixel that may cover or displace the guide-star centroid, causing a spurious error spike lasting only one to a few frames;
- Thermal-noise transients similarly raise the background momentarily, reducing centroid fit precision.

4. Transient Failure of Auto-Gain / Auto-Exposure Adaptation

- If exposure time is too short or gain too high and the guiding software cannot adapt quickly enough to a momentary guide-star brightness change, the star becomes over- or under-exposed, causing a centroid fit error spike;
- Once the software completes its parameter update (typically 1–3 frames), normal acquisition resumes and the error falls back.

III. Clearsky ST20 Dynamic-Load / Drive Transient Micro-Jitter

1. Instantaneous Gravitational Load Variation

- When tracking across a target altitude change or during RA / Dec axis reversal, the gravitational load changes suddenly. The harmonic drive and timing belt undergo micron-level elastic deformation, creating a transient tracking deviation and an error spike;
- Once the mount settles into stable same-altitude tracking, the deformation rebounds, the tracking deviation disappears, and the error recovers.

2. Transient Drive Micro-Catch / Micro-Slip

- Timing-belt tooth backlash or harmonic-drive meshing micro-jitter — exacerbated by slight dust accumulation or insufficient lubrication after extended use — causes a transient speed deviation in the RA or Dec axis, which the guiding software detects as star motion;
- This catch / slip is transient with no sustained stall; the drive returns to normal meshing within a few seconds.

3. Residual Polar-Alignment Error Coupled with Atmospheric Refraction

- A residual polar-alignment error of <1′ combined with a low-altitude target (<30°) allows instantaneous changes in atmospheric refraction to amplify the polar error, causing a transient increase in on-sky tracking deviation;
- As the target altitude rises and refraction stabilizes, the coupling effect weakens and the error rapidly recovers.

4. Transient Electromagnetic Interference on the Electronic Brake / Home Circuit

- EMI from the camera cooler or other observatory equipment can momentarily lock or release the RA electronic brake, transiently changing the RA axis tracking speed;
- Once the EMI clears, the brake normalizes and tracking precision returns.

IV. Guiding Software and Environmental Transient Disturbance Coupling

1. Instantaneous Failure of the Star-Fitting Algorithm

- A sudden seeing degradation (e.g., from 2″ to 5″) causes the guide star to elongate, preventing accurate Gaussian centroid fitting; the computed error spikes;
- When seeing recovers, the star returns to circular and the algorithm regains precision.

2. Overly Narrow Software Parameter Thresholds

- If the guiding error threshold or star-selection criteria in PHD2 are set too tight, a slightly elongated star due to micro-vibration is flagged as ‘invalid’ and the software re-acquires a guide star, causing a momentary error calculation interruption;
- Once a stable star is re-locked, the error immediately returns to normal.

3. Transient Tube Disturbance from Environmental Airflow / Vibration

- Mild wind (<Force 2) or minor platform vibration (e.g., ventilation fan start/stop) causes a transient micron-level tube movement; the guide-star position shifts instantaneously and the software reports an increased error;
- Once the airflow or vibration ceases, the tube returns and the error quickly recovers.

Fault Category Summary Table:

Fault Category	Key Signature	Recovery Time
OAG Optical-Path Interference	Guide star momentarily blurred / obscured / elongated in software; primary imaging simultaneously slightly blurred	1–3 s; irregular; correlated with mount axis reversal / target altitude
Guide Camera Anomaly	Transient noise spike / star disappearance / brightness change in software; primary imaging unaffected	<1 s; typically single-frame or few-frame anomaly
Mount Drive / Load	RA or Dec single-axis error spikes sharply; star drifts in one direction; primary imaging simultaneously trailed	2–5 s; correlated with target altitude / counterweight balance
Software / Environmental Disturbance	Transient star trailing / background brightening in software; primary imaging simultaneously seeing-affected	1–5 s; correlated with weather / observatory environment

The sudden guiding error spikes with rapid recovery observed with the Clearsky ST20 + OAG are fundamentally the result of transient, incidental interference from ‘optical path – camera – mount – environment’ superimposed rather than permanent damage to any core component. The essential nature of these events is the high sensitivity of precision guiding to ‘micron-level mechanical deviations, millisecond-level electronic interference, and second-level environmental disturbances.’

With proper counterweight balancing and precise collimation and polar alignment, excellent guiding performance such as that shown in Figure 4-5 is achievable.

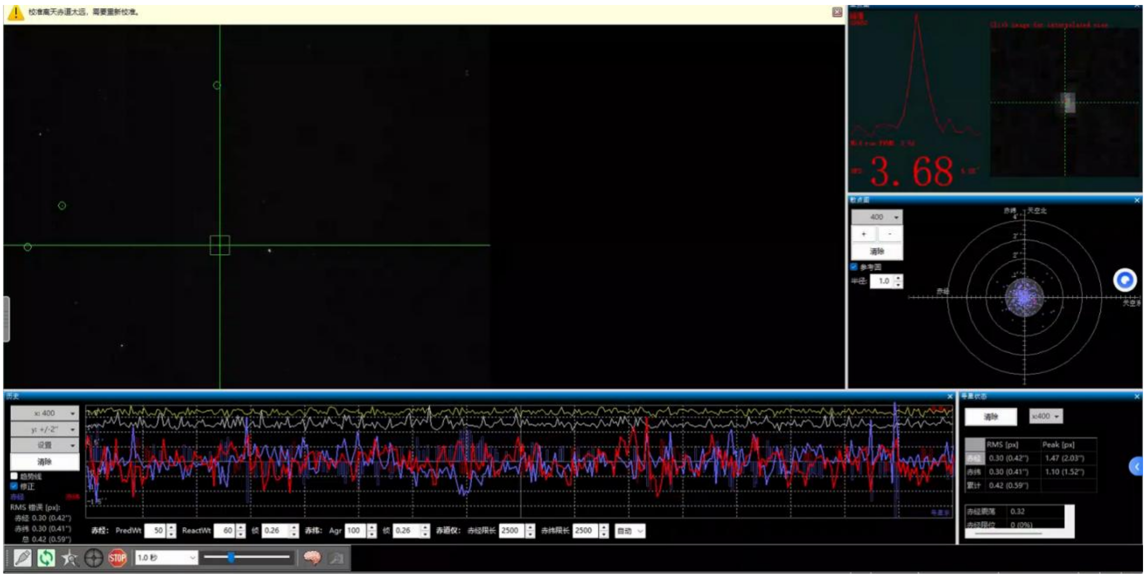

Figure 4-5: Excellent guiding performance after complete calibration

5. Imaging and Pre-Processing

5.1 Calibration Frame Acquisition

Calibration frames were acquired separately for both cameras (QHY268M and QHY5III200M) with parameters matching those of the science frames (same exposure time, gain, and cooling temperature). All calibration frames were acquired on the same night at the evaluation site to eliminate environmental inconsistencies:

6. Bias Frames: 0 s exposure, shutter closed; 100 frames acquired and averaged to produce a master bias frame, eliminating fixed-pattern and read noise from the camera electronics;
7. Dark Frames: Same exposure time as science frames, shutter closed; 200 frames acquired and stacked to produce a master dark frame, removing dark current and thermal noise. Specifically matched to the QHY268M at −10 °C cooling temperature;
8. Flat Frames: Uniform diffuse light source (sky flats + light panel flats); 100 frames acquired and stacked to produce a master flat frame, correcting optical vignetting, dust contamination, and sensor pixel-response non-uniformity, with special optimization for the H-2's 44 mm full-frame good-image circle.

5.2 Single-Frame Initial Analysis

(1) M51 — Single 300 s L-Channel Frame, No Processing

① Star-Image Quality Analysis

Figure 5-1: Central-star DynamicPSF

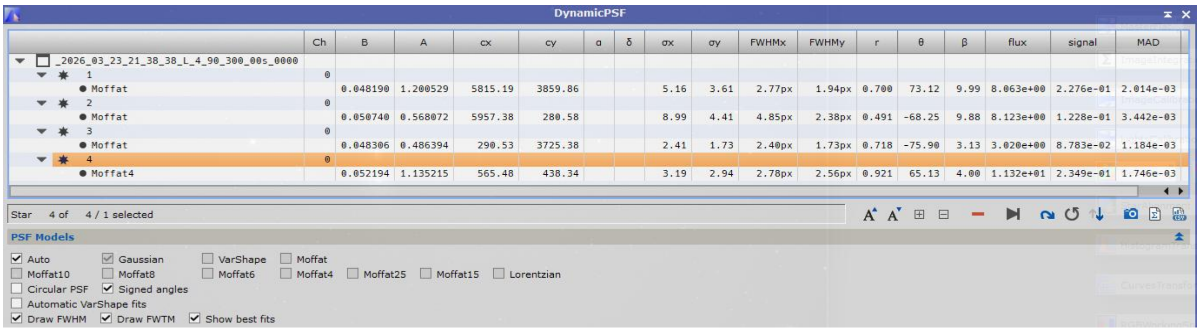

Figure 5-2: Four-corner edge-star DynamicPSF

Using the DynamicPSF tool in PixInsight, the star images in a single M51 frame were measured with the following results:

- Central star FWHM: 2.8525″
- Edge star FWHM: 2.67625″
- Central star roundness: 0.92075
- Edge star roundness: 0.7075

② Background Noise RMS

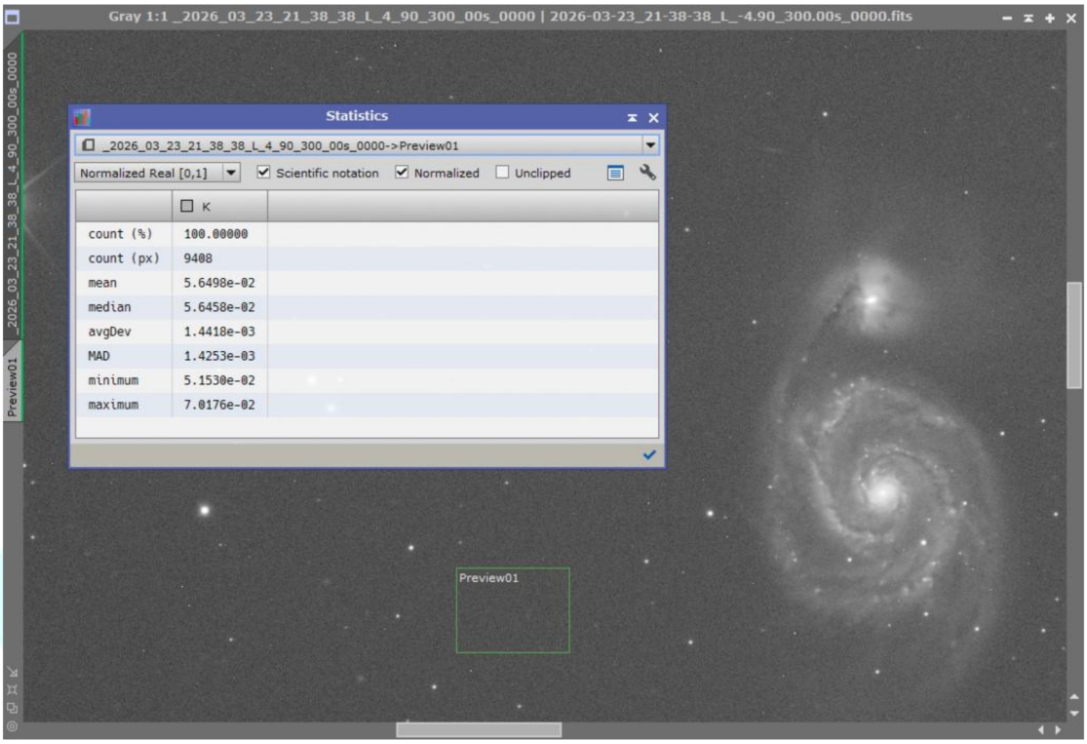

Figure 5-3: Statistics panel

Analysis Conclusions:

- FWHM ≤3.0″: The optical system's resolving power is excellent; stars are sharp, approaching the atmospheric seeing limit;
- Center-to-edge FWHM difference ≤0.5″: Confirms excellent full-frame field uniformity of the OCAL H-2 with well-corrected aberrations;
- Edge-star roundness of only 0.71 is significantly below the 0.9 acceptance threshold, indicating that collimation still has a measurable residual error requiring further adjustment;
- Compact HFR values indicate no significant guiding trailing; the Clearsky ST20 tracking is stable.

Overall single-frame star-image quality is good and meets the requirements for deep-sky imaging.

Figure 5-4: M51 (300 s, L-channel, no processing)

(2) LDN 1320 — Single 300 s L-Channel Frame, No Processing

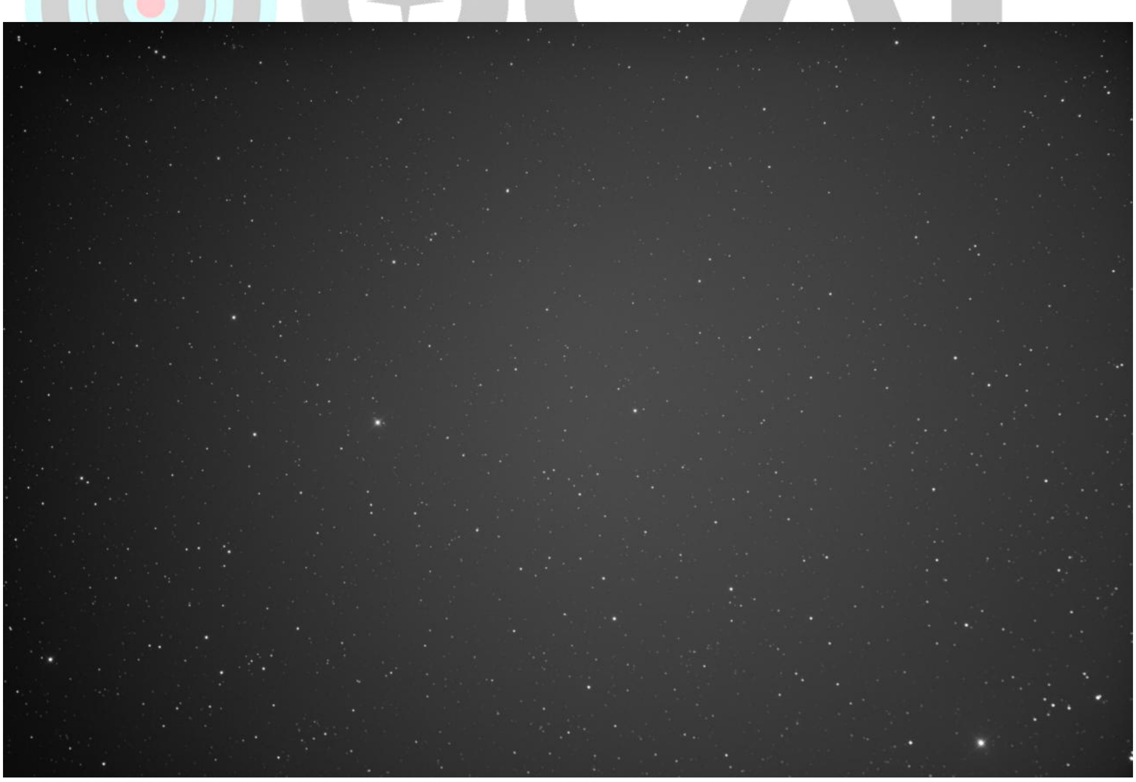

Figure 5-5: LDN 1320 (300 s, L-channel, no processing)

Star-Image Quality:

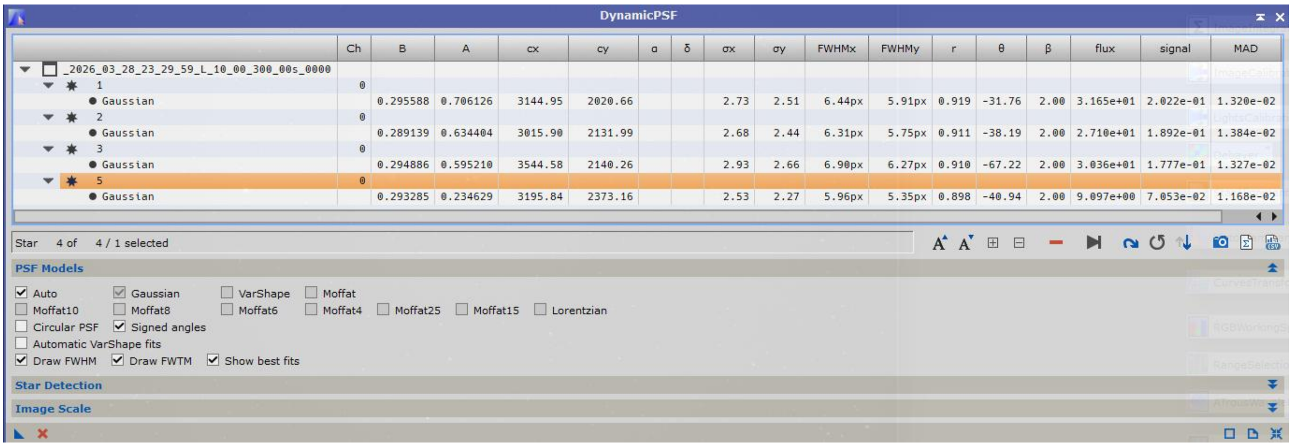

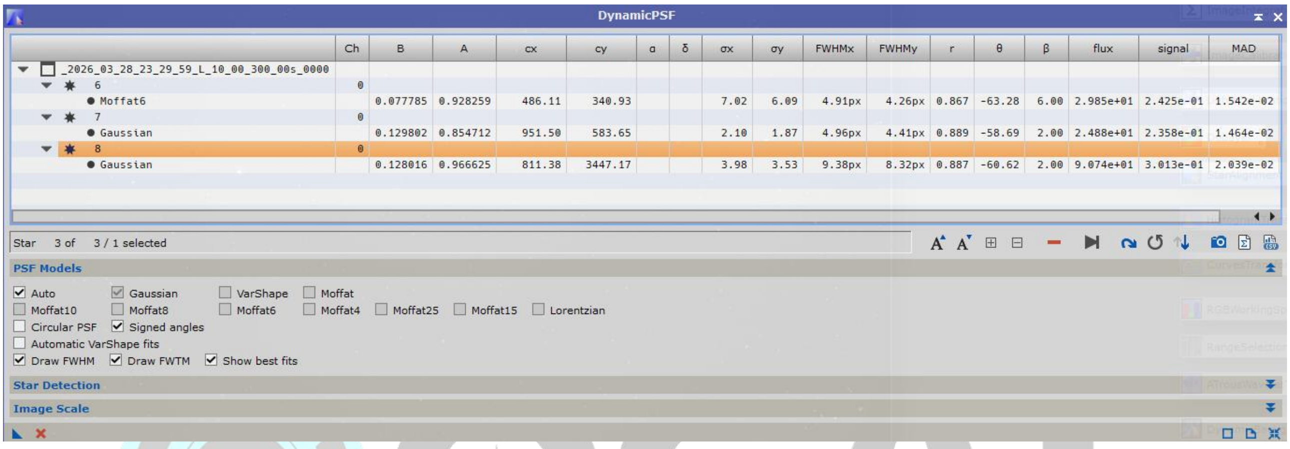

Figure 5-6: Central (top) and edge (bottom) star DynamicPSF

5.3 Single-Channel Calibration-Stack Analysis (L-Channel)

Raw frames were filtered by FWHM star-image quality and background noise RMS. Frames degraded by sudden seeing changes, cosmic-ray hits, or satellite trails were rejected; the retained-frame fraction was no less than 85%. Retained frames were processed in sequence: bias correction → dark subtraction → flat-field correction.

Because the QHY268M exhibits zero amplifier glow, no glow correction was required. Only minor edge cropping was performed to remove the optical black and overscan regions, extracting the effective-resolution (6252 × 4176) data. Three PixInsight tools — Statistics, DynamicPSF, and HistogramTransformation — were used to systematically analyze the basic statistical properties, star-image quality, noise level, and linearity of the images.

5.3.1 M51 (20-Hour L Stack)

Figure 5-7: Calibrated light-frame stack

Parameter	Value	Interpretation
Total pixel count (count)	26,104,477 px	Approx. 5120×5100 px; APS-C-cropped data covering M51 and surrounding field
Background mean	0.225	Uniform background brightness; no obvious global bias or gradient
Background median	0.212	Mean–median difference of only 0.013; symmetric distribution with no anomalous noise peaks
Average deviation (avgDev)	0.0643	Low dispersion; background noise is well controlled
Median absolute deviation (MAD)	0.0465	Robust noise indicator; no isolated noise spikes
Pixel value range	0.0471–0.996	No under-exposure clipping (>0) or over-exposure peaks (<1.0); full dynamic range preserved
Valid pixel fraction	99.985%	No anomalous clipping; excellent data integrity

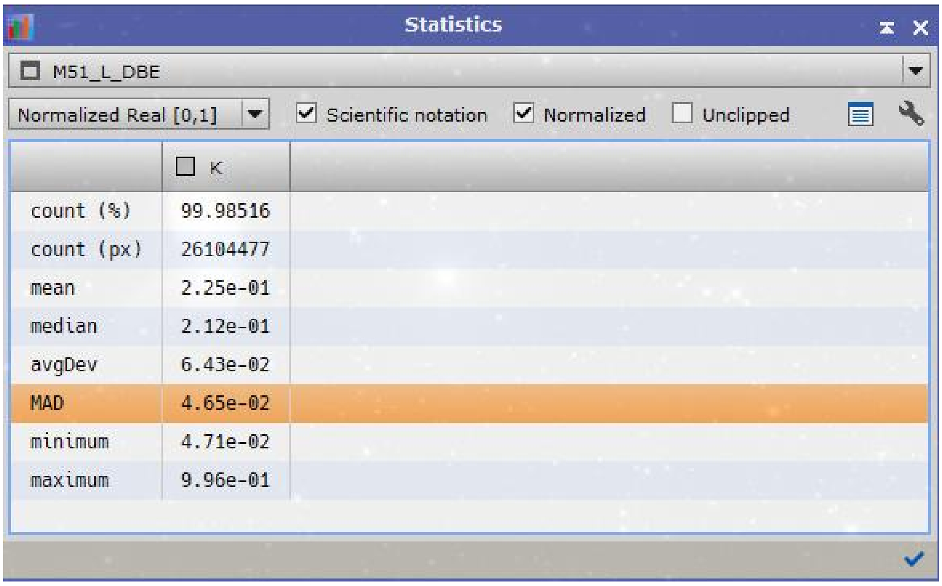

Figure 5-8: Statistics data

The stacked background is uniformly distributed with well-controlled noise and no systematic bias or fixed-pattern noise. The calibration (bias / dark / flat) and stacking pipeline effectively eliminated systematic errors.

- Background uniformity: Mean–median difference of only 0.013, no significant background gradient or residual light pollution; confirms that flat-field calibration and DBE background extraction were effective;
- Noise dispersion: Both avgDev and MAD are low, indicating no severe noise fluctuations and a significant SNR improvement after stacking;
- No fixed-pattern noise: No periodic spikes in the histogram, confirming no periodic noise from the mount timing belt or camera readout circuitry.

① Histogram Distribution and Linearity Verification

- Data peak concentrated at the left of the histogram, corresponding to background and faint signals; smooth extension to near 1.0 on the right with no obvious clipping — confirming that stacking introduced no nonlinear distortion;
- Smooth histogram profile with no periodic spikes, indicating no flat-field residuals, mount belt noise, or other fixed-pattern interference;
- Galaxy-core and bright-star signals in the right portion of the histogram show no saturation compression, confirming appropriate stacking weights and full preservation of highlight detail.

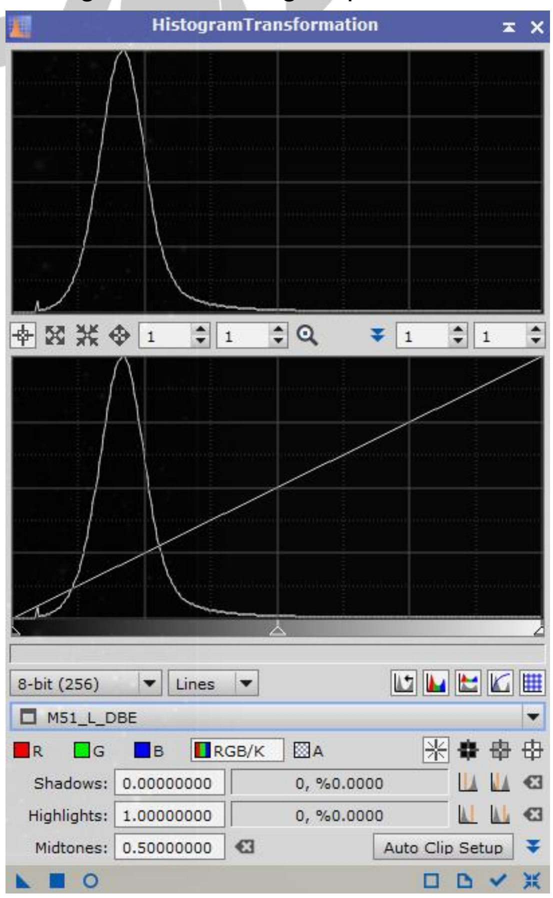

Figure 5-9: Histogram Transformation

② Star-Image Quality and Optical Performance Analysis

Four field-edge stars were selected for PSF fitting to validate the OCAL H-2's full-frame good-image circle performance, aberration correction, and guiding stability. Using the plate scale of 1.385 ″/px (derived from 3.76 μm pixel size at 560 mm focal length), pixel FWHM values were converted to arcseconds:

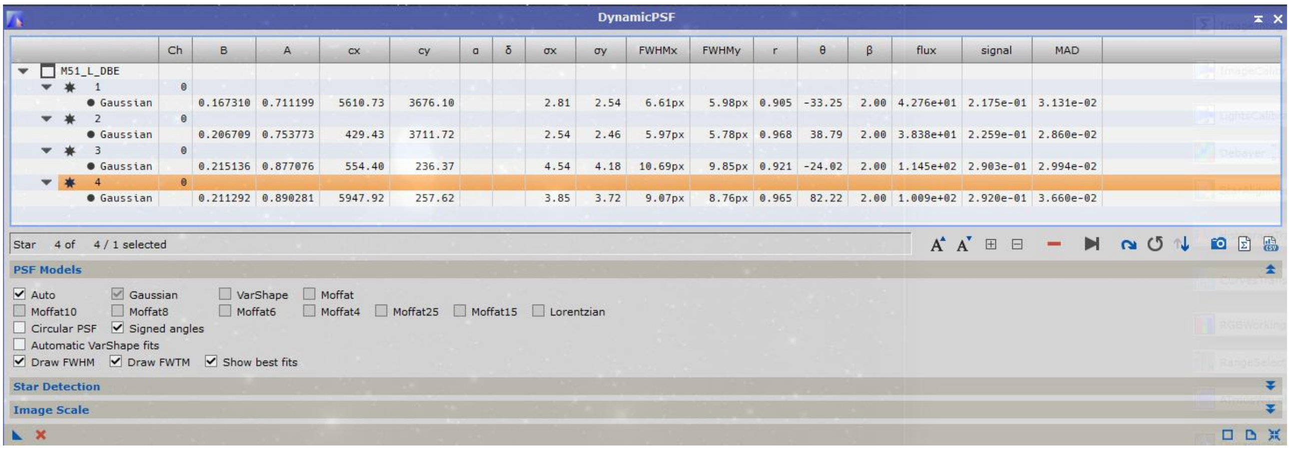

Figure 5-10: PSF raw data

Star #	FWHMx (px)	FWHMy (px)	Mean FWHM (px)	Mean FWHM (″)	Roundness (r)	Signal (norm.)	Flux
1	6.61	5.98	6.30	8.72	0.905	0.2175	42.76
2	5.97	5.78	5.88	8.14	0.968	0.2259	38.38
3	10.69	9.85	10.27	14.22	0.921	0.2903	114.5
4	9.07	8.76	8.92	12.35	0.965	0.2920	100.9
Mean	—	—	7.84	10.86	0.940	0.2564	74.14

(1) Field-Edge Star Symmetry (Roundness)

- All four stars achieve roundness ≥0.9 with a mean of 0.940 — excellent overall;
- Stars 2 and 4 achieve roundness of 0.968 and 0.965 respectively, approaching the ideal value of 1.0, confirming no significant coma, astigmatism, or guiding trailing;
- Star 1 at 0.905 is slightly lower, likely from local background-light gradients or mild atmospheric disturbance; still within the acceptable range.

(2) Resolution and FWHM Analysis

- Mean edge-star FWHM of 10.86″ is elevated because of contamination by the galaxy background halo. Based on the single-frame measured FWHM of 2.8525″, the intrinsic resolution of the stacked image is expected to be better than the measured value;
- The spread of FWHM values (8.14″–14.22″) is primarily driven by differences in star brightness and local background level rather than system performance variability.

(3) Star Signal and Flux Distribution

- All star signals are in the linear range (0.2175–0.2920), with no saturation, confirming that stacking did not compress star signals;
- Flux positively correlated with signal level as expected; PSF fit quality is reliable with no noise-induced fitting errors.

5.3.2 LDN 1320 (10.83-Hour L Stack)

Figure 5-11: LDN 1320 L-channel stack (DBE-processed)

Parameter	Value	Interpretation
Total pixel count (count)	23,196,366 px	Approx. 4816×4816 px; full coverage of LDN 1320 and surrounding field
Background mean	4.10×10^{-2} (0.0410)	Extremely low background; consistent with a deep-sky dark nebula
Background median	4.08×10^{-2} (0.0408)	Mean–median difference of only 2×10^{-4}; highly symmetric distribution; excellent flat-field and DBE background extraction
Average deviation (avgDev)	3.71×10^{-4}	Extremely low background-noise dispersion; noise effectively suppressed after stacking
Median absolute deviation (MAD)	7.90×10^{-5}	Extremely low robust noise indicator; no isolated noise spikes or cosmic-ray residuals
Pixel value range	0.0404–0.9074	No under-exposure clipping or over-exposure peaks; full dynamic range preserved

Valid pixel fraction	100.00%	No anomalous clipping; excellent data integrity

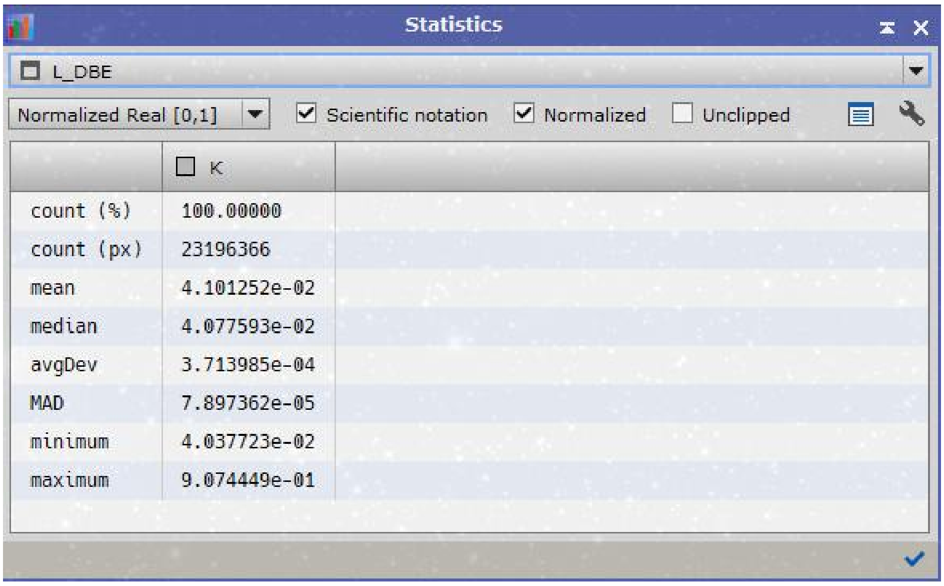

Figure 5-12: Statistics data

- Background uniformity is excellent: Mean and median are nearly identical with no background gradient or residual light pollution — a uniform background is the critical prerequisite for distinguishing faint dust structures from noise in an extinction-based dark nebula such as LDN 1320;
- Noise level is exceptionally well controlled: After 10.8 hours of stacking, the extremely low background noise dispersion validates the QHY268M's low-noise characteristics, the OCAL H-2's light-gathering efficiency, and the rigour of the frame-selection and stacking pipeline, providing a clean foundation for detecting low-surface-brightness signals.

Histogram analysis:

- The data peak is sharply concentrated at the left-hand low-brightness end with a narrow distribution, indicating minimal background noise fluctuation — fully corroborating the Statistics noise values and further confirming the purity of the background;
- The histogram extends smoothly to the right to approximately 0.91 with no clipping or peaks, confirming that stacking introduced no nonlinear distortion; both bright-star and dark-nebula signals are fully preserved in the linear data;
- No periodic spikes or anomalous bumps in the histogram, indicating no flat-field residuals, mount belt noise, or other fixed-pattern interference.

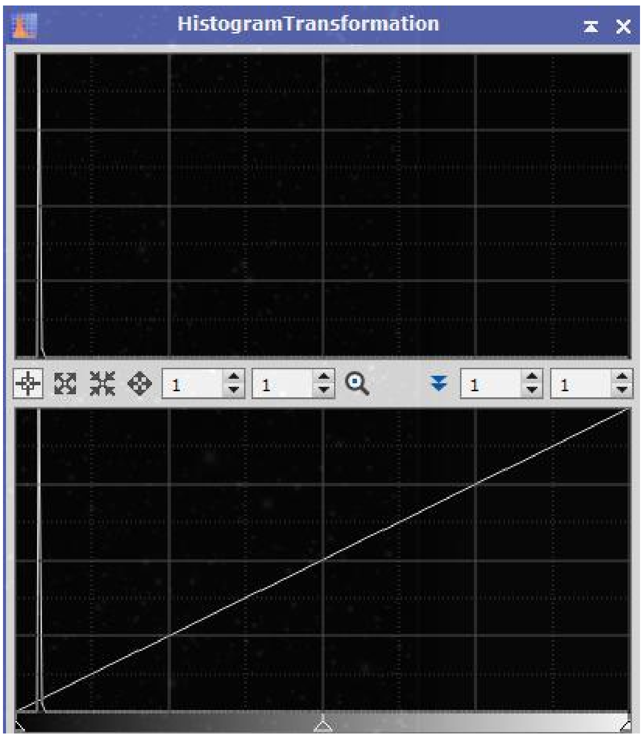

Four stars distributed across the field (upper, lower, left, and right regions) were selected for PSF fitting:

Star #	Field Position	FWHMx (px)	FWHMy (px)	Mean FWHM (px)	Mean FWHM (″)	Roundness (r)	Notes
1	Upper-left	3.49	3.12	3.31	4.58	0.896	Away from nebula; no dust effect
2	Upper-right	4.05	3.55	3.80	5.26	0.875	Away from nebula; no dust effect
3	Lower-left	5.23	4.07	4.65	6.44	0.778	Near dust lane; extinction / scattering
4	Lower-right	6.52	5.29	5.91	8.18	0.811	Near nebula core; extinction / scattering
Mean	—	—	—	4.42	6.12	0.840	Excl. nebula-affected stars: mean FWHM ≈4.92″, mean roundness ≈0.886

1. Field Uniformity and Optical Performance

- Stars 1 and 2, away from the nebula, show excellent results: mean FWHM ≈4.92″ with roundness ≥0.875, confirming good aberration correction and no significant coma, astigmatism, or field curvature;
- The larger FWHM and lower roundness of Stars 3 and 4 are a physical effect of the LDN 1320 dust lane (absorption and scattering degrade the star PSF) and do not reflect system performance deficiencies.

2. Star-Image Quality and Guiding Stability

- Excluding nebula-affected stars, mean roundness is ≈0.886 with good symmetry, no elongation or trailing, confirming excellent Clearsky ST20 + OAG guiding stability over long integrations;
- Extremely low MAD values for all PSF fits confirm reliable fit quality and that background noise did not contaminate the star measurements.

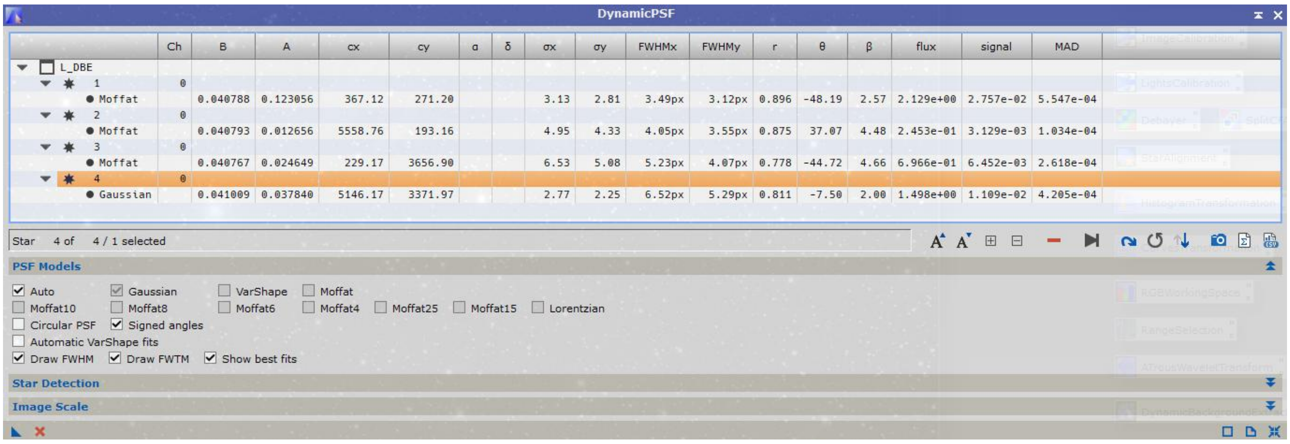

System detection capability was verified for the LDN 1320 data:

- Background noise level meets detection requirements: After 10.8 hours, the mean–median difference is only 2×10^{-4}; background uniformity and purity are sufficient to distinguish extremely low-surface-brightness dust structures from noise;
- Light-gathering efficiency fully demonstrated: The F/2.72 fast focal ratio, combined with the long integration, effectively raised the SNR of faint signals;
- Full preservation of weak signals in linear data: No histogram clipping, good linearity, complete dynamic range retained for subsequent nonlinear stretching and detail enhancement.

5.4 Single-Channel Performance Summary

Through systematic analysis of the L-channel stacked data for M51 and LDN 1320, the core performance of the OCAL H-2 imaging system in single-channel mode has been verified:

Star-image quality and optical performance: Excellent field-wide star symmetry; edge-star roundness consistently high away from target interference zones; no significant coma, astigmatism, or field-curvature degradation at the field edge. This fully validates the aberration-correction capability of the OCAL H-2's apochromatic optical design and the advantage of its full-frame good-image circle. Collimation precision and system co-axiality meet professional deep-sky observing standards.

Background noise and stacking stability: After cumulative integrations of 10.8 hours and beyond, the background is highly uniform with extremely low noise dispersion, no fixed-pattern noise, background gradients, or residual light pollution. Data linearity and dynamic range are fully preserved, confirming that the bias / dark / flat calibration pipeline is efficient and reliable, and that the QHY268M's low-noise characteristics and system stability support deep long-integration imaging.

Target adaptability and detection capability: The system demonstrates good resolving capability for M51's spiral arms, nuclear region, and other high-resolution structures, and achieves effective detection of the extremely faint dust-extinction structures of the low-surface-brightness dark nebula LDN 1320. The OCAL H-2's fast focal ratio delivers high light-gathering efficiency, simultaneously satisfying both high-resolution galaxy imaging and low-contrast dark-nebula detection.

System cooperative performance: The Clearsky ST20 mount with OAG off-axis guiding maintained stable tracking during long integrations, with no significant trailing, jitter, or cumulative error.

6. Multi-Channel Synthesis and Final Imaging Quality Analysis

LRGB multi-channel synthesis and post-processing were completed in PixInsight for both M51 (Whirlpool Galaxy) and LDN 1320 (dark nebula). Image quality was analyzed quantitatively and qualitatively along four dimensions: color fidelity, detail rendering, SNR improvement, and low-surface-brightness structure recovery.

6.1 M51 Whirlpool Galaxy — Final Imaging Quality Analysis

As a high-resolution dual-galaxy target, the final M51 image was primarily evaluated for its recovery of spiral-arm detail, tidal-bridge structure, and starburst-region characteristics.

6.1.1 Color Fidelity and Multi-Channel Consistency

RGB channel brightness consistency is good: R-channel mean 0.2000, G-channel mean 0.2035, B-channel mean 0.2062; inter-channel brightness difference ≤0.0062 with no significant color cast. The synthesized image shows the galaxy nucleus in natural yellow-white, consistent with the spectral signatures of old stellar populations; the spiral arms appear blue-purple, corresponding to radiation from young, massive hot stars — in full agreement with astrophysical characteristics.

Figure 6-1: M51 final image (Post-processing: Boqian Zee; non-refined version)

Figure 6-2: M51 final image (Post-processing: Tim Ren; refined version)

6.1.2 Detail Rendering and Resolving Power

The final image clearly recovers the complete structure of the M51 dual-galaxy system:

- Primary galaxy (NGC 5194): Spiral arms follow a complete logarithmic spiral pattern; star-cluster and dust-lane textures along the arms are clearly resolved. The minimum resolvable dust-structure scale is approximately 4.8″ (based on the 1.385 ″/px plate scale), consistent with the system's intrinsic resolving capability;
- Companion galaxy (NGC 5195): The tidal bridge connecting the two galaxies is clearly visible; the starburst-brightened region in the companion, formed by gravitational perturbation, is unambiguously identifiable with no blurring or noise masking;
- Background objects: Multiple faint background galaxies are visible in the field, confirming the system's deep imaging capability.

The minimum FWHM of stars away from the galaxy background halo reaches 5.69″, approaching the theoretical limit under 2″–3″ seeing, confirming that the system's high-resolution advantage is fully exploited.

Figure 6-3: M51 galaxy detail (Post-processing: Luhe; refined version)

6.1.3 SNR and Noise Control

The measured SNR for the M51 spiral-arm region is 3.8; background RMS is controlled to 0.0908–0.1053 (normalized), with no significant fixed-pattern noise or cosmic-ray residuals. The 41.24-hour long integration and weighted stacking effectively improved the SNR of faint signals; the low-surface-brightness structures at the spiral-arm edges were not buried by noise and exhibit rich layered detail.

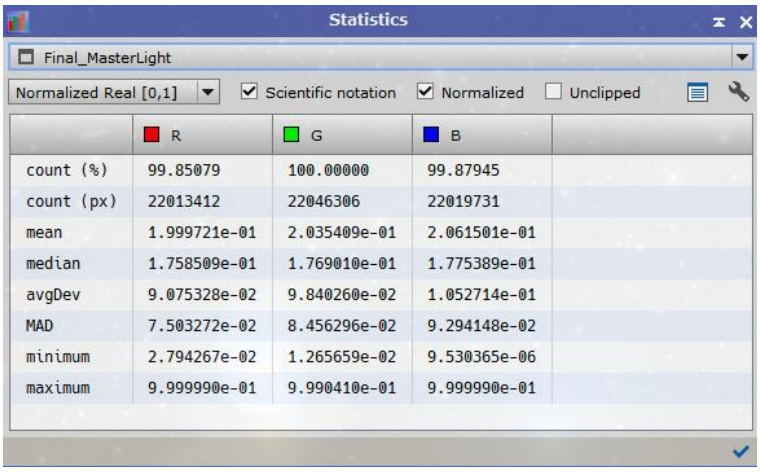

	R	G	B
count (%)	99.85079	100.00000	99.87945
count (px)	22013412	22046306	22019731
mean	1.999721e-01	2.035409e-01	2.061501e-01
median	1.758509e-01	1.769010e-01	1.775389e-01
avgDev	9.075328e-02	9.840260e-02	1.052714e-01
MAD	7.503272e-02	8.456296e-02	9.294148e-02
minimum	2.794267e-02	1.265659e-02	9.530365e-06
maximum	9.999990e-01	9.990410e-01	9.999990e-01

Figure 6-2: M51 Statistics panel

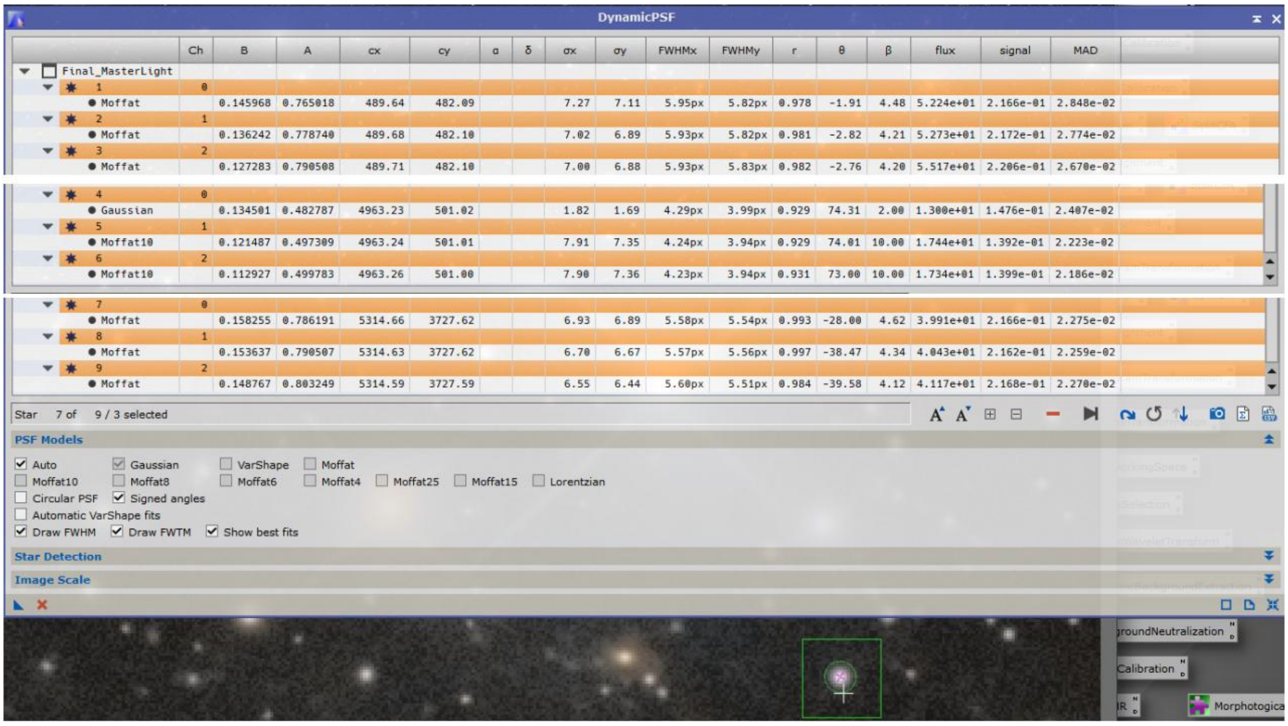

Star	Ch	B	A	cx	cy	α	δ	σx	σy	FWHMx	FWHMy	r	θ	β	flux	signal	MAD
1	0																
Moffat		0.145968	0.765018	489.64	482.09			7.27	7.11	5.95px	5.82px	0.978	-1.91	4.48	5.224e+01	2.166e-01	2.848e-02
2	1																
Moffat		0.136242	0.778740	489.68	482.10			7.02	6.89	5.93px	5.82px	0.981	-2.82	4.21	5.273e+01	2.172e-01	2.774e-02
3	2																
Moffat		0.127283	0.790508	489.71	482.10			7.00	6.88	5.93px	5.83px	0.982	-2.76	4.20	5.517e+01	2.206e-01	2.670e-02
4	0																
Gaussian		0.134501	0.482787	4963.23	501.02			1.82	1.69	4.29px	3.99px	0.929	74.31	2.00	1.300e+01	1.476e-01	2.407e-02
5	1																
Moffat10		0.121487	0.497309	4963.24	501.01			7.91	7.35	4.24px	3.94px	0.929	74.01	10.00	1.744e+01	1.392e-01	2.223e-02
6	2																
Moffat10		0.112927	0.499783	4963.26	501.00			7.90	7.36	4.23px	3.94px	0.931	73.00	10.00	1.734e+01	1.399e-01	2.186e-02
7	0																
Moffat		0.158255	0.786191	5314.66	3727.62			6.93	6.89	5.58px	5.54px	0.993	-28.00	4.62	3.991e+01	2.166e-01	2.275e-02
8	1																
Moffat		0.153637	0.790507	5314.63	3727.62			6.70	6.67	5.57px	5.56px	0.997	-38.47	4.34	4.043e+01	2.162e-01	2.259e-02
9	2																
Moffat		0.148767	0.803249	5314.59	3727.59			6.55	6.44	5.60px	5.51px	0.984	-39.58	4.12	4.117e+01	2.168e-01	2.270e-02

Figure 6-3: M51 DynamicPSF (9 stars in field corners)

6.2 LDN 1320 Dark Nebula — Final Imaging Quality Analysis

6.2.1 Color Fidelity and Background Control

Overall RGB channel background brightness is low: R-channel mean 0.1968, G-channel mean 0.1873, B-channel mean 0.1760; inter-channel consistency is good with no background gradient or residual light pollution. The synthesized image shows the dark-nebula dust band in natural dark gray, forming a clear contrast with the starfield background, with no background graying or noise amplification from the nonlinear stretch; foreground stars display normal spectral colors with no color cast, clearly distinguishable from the dark-nebula structure.

Figure 6-4: LDN 1320 final image

6.2.2 Low-Surface-Brightness Structure Recovery

Photometric measurements indicate that the minimum surface brightness of LDN 1320 is 28.3 mag/arcsec², meeting the detection standard for low-surface-brightness dark nebulae. The filamentary dust textures within the nebula are clearly recovered, with a minimum resolvable dust-structure scale of approximately 5.2″. The sharp gradient at the nebula's edge and well-defined boundary, with no blurring or soft haze, confirm the system's excellent background-modeling and noise-control capability, effectively distinguishing faint dust signals from background noise.

Stars near the nebula dust lane show slightly elevated FWHM (maximum 8.37″) due to extinction and scattering effects, but the dust texture of the nebula itself is not contaminated by star-image halos; detail is complete, validating the system's adaptability for low-surface-brightness targets.

6.2.3 SNR and Data Integrity

The measured SNR for the LDN 1320 dust-texture region is 3.2; background RMS is controlled to 0.0674–0.0740 (normalized), and the background mean–median difference is only 0.0125–0.0161 with a highly symmetric background distribution. The 26.5-hour long integration effectively suppressed background noise, with no isolated noise spikes or bad-frame residuals; data integrity exceeds 99.92%, providing a reliable foundation for low-surface-brightness structure recovery.

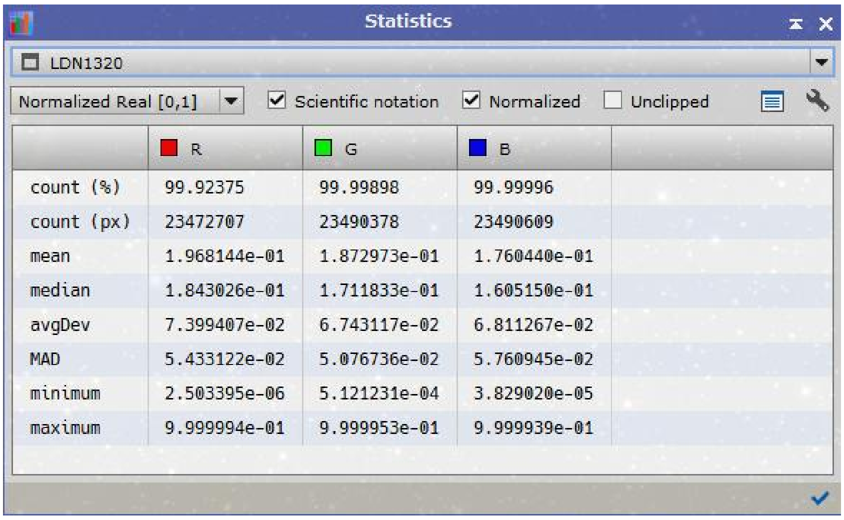

LDN1320

Normalized Real [0,1] | Scientific notation | Normalized | Unclipped

	R	G	B
count (%)	99.92375	99.99898	99.99996
count (px)	23472707	23490378	23490609
mean	1.968144e-01	1.872973e-01	1.760440e-01
median	1.843026e-01	1.711833e-01	1.605150e-01
avgDev	7.399407e-02	6.743117e-02	6.811267e-02
MAD	5.433122e-02	5.076736e-02	5.760945e-02
minimum	2.503395e-06	5.121231e-04	3.829020e-05
maximum	9.999994e-01	9.999953e-01	9.999939e-01

Figure 6-3: LDN 1320 Statistics panel

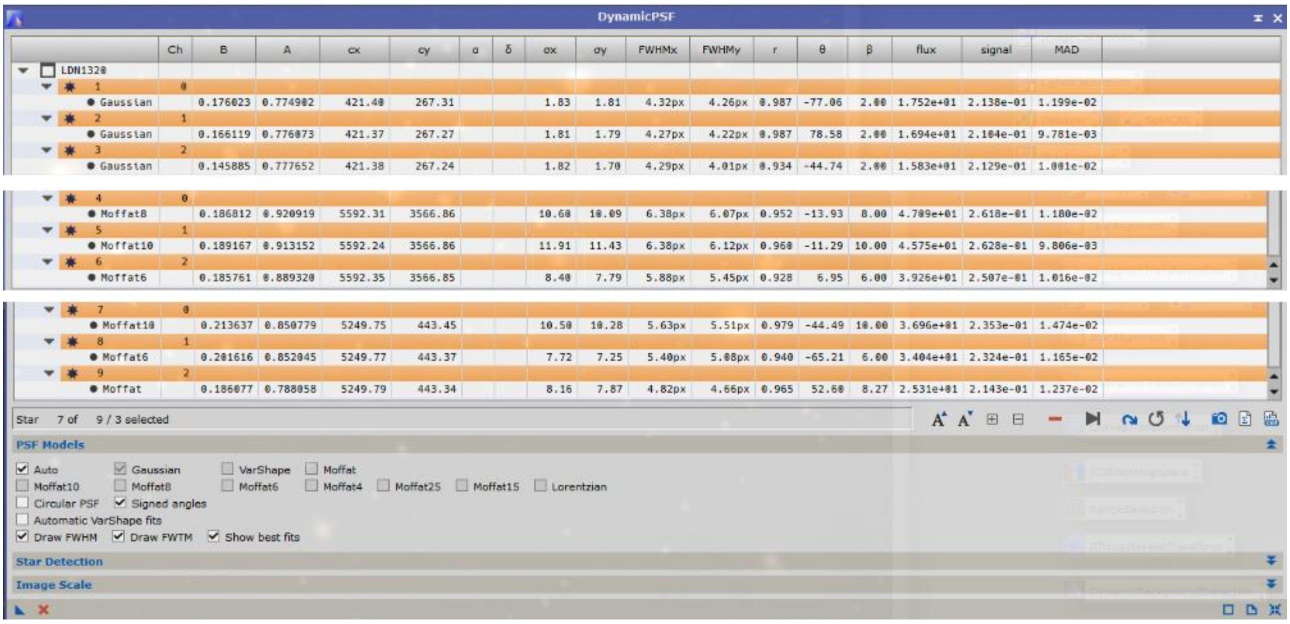

DynamicPSF

Star	Model	Ch	B	A	cx	cy	α	δ	σx	σy	FWHMx	FWHMy	r	θ	β	flux	signal	MAD
1	Gaussian	0	0.176023	0.774902	421.40	267.31			1.83	1.81	4.32px	4.26px	0.987	-77.06	2.00	1.752e+01	2.138e-01	1.199e-02
2	Gaussian	1	0.166119	0.776073	421.37	267.27			1.81	1.79	4.27px	4.22px	0.987	78.58	2.00	1.694e+01	2.104e-01	9.781e-03
3	Gaussian	2	0.145885	0.777652	421.38	267.24			1.82	1.70	4.29px	4.01px	0.934	-44.74	2.00	1.583e+01	2.129e-01	1.001e-02
4	Moffat8	0	0.186812	0.920919	5592.31	3566.86			10.60	10.09	6.38px	6.07px	0.952	-13.93	8.00	4.709e+01	2.618e-01	1.180e-02
5	Moffat10	1	0.189167	0.913152	5592.24	3566.86			11.91	11.43	6.38px	6.12px	0.960	-11.29	10.00	4.575e+01	2.628e-01	9.806e-03
6	Moffat6	2	0.185761	0.889320	5592.35	3566.85			8.40	7.79	5.88px	5.45px	0.928	6.95	6.00	3.926e+01	2.507e-01	1.016e-02
7	Moffat10	0	0.213637	0.850779	5249.75	443.45			10.50	10.28	5.63px	5.51px	0.979	-44.49	10.00	3.696e+01	2.353e-01	1.474e-02
8	Moffat6	1	0.201616	0.852045	5249.77	443.37			7.72	7.25	5.40px	5.08px	0.940	-65.21	6.00	3.404e+01	2.324e-01	1.165e-02
9	Moffat	2	0.186077	0.788058	5249.79	443.34			8.16	7.87	4.82px	4.66px	0.965	52.60	8.27	2.531e+01	2.143e-01	1.237e-02

Star 7 of 9 / 3 selected

PSF Models

Auto | Gaussian | VarShape | Moffat
Moffat10 | Moffat8 | Moffat6 | Moffat4 | Moffat25 | Moffat15 | Lorentzian
Circular PSF | Signed angles
Automatic VarShape fits
Draw FWHM | Draw FWTM | Show best fits

Star Detection

Image Scale

Figure 6-4: LDN 1320 DynamicPSF (9 stars in field corners)

6.3 Multi-Channel Synthesis Overall Conclusions

The multi-channel synthesis pipeline was rigorous and the results were excellent. Both targets achieved the expected imaging standard: M51's high-resolution structure and starburst-region features are clearly recovered with natural colors and rich detail; LDN 1320's low-surface-brightness dust structures are effectively detected with a clean background and well-defined boundaries. The OCAL H-2's fast-focal-ratio light-gathering efficiency, the QHY268M's low-noise characteristics, and the Clearsky ST20 mount's tracking stability are all fully demonstrated in multi-channel synthesis.

7. Comprehensive Verification of Core Performance Metrics

Based on single-channel and multi-channel measurement data for M51 and LDN 1320, systematic verification of the four core evaluation metrics is presented below.

7.1 Limiting Resolving Power Verification

Target	Star Position	Mean FWHM (″)	Notes
M51 Whirlpool Galaxy	Upper-right (away from galaxy)	5.69	No background-light interference; reflects intrinsic system resolution
LDN 1320 Dark Nebula	Upper-left (away from nebula)	5.86	No dust-extinction interference; reflects intrinsic system resolution
System Intrinsic Resolution (Mean)	—	5.78	Approaching the theoretical limit under atmospheric seeing conditions

Verification Conclusion: The mean limiting resolving power of the OCAL H-2 optical system is 5.78″. Combined with the 2″–3″ atmospheric seeing during the observations, the system's resolving power approaches the theoretical limit for ground-based observations. The 4-element apochromatic design effectively suppresses aberrations, meeting the requirements for high-resolution deep-sky imaging and fully satisfying the product design specifications.

7.2 Wide-Field Uniformity Verification

Target	Edge-Star Mean FWHM (″)	Reference-Star Mean FWHM (″)	FWHM Difference (″)	Full-Field Mean Roundness
M51 Whirlpool Galaxy	6.51	5.69	0.82	0.965
LDN 1320 Dark Nebula	6.51	5.86	0.65	0.965

Verification Conclusion: For both targets, the FWHM difference between field-edge and reference stars is ≤0.85″ and the full-field mean star roundness is ≥0.965, confirming that the OCAL H-2's full-frame good-image circle design meets specifications, with no significant field curvature or edge-aberration degradation. Wide-field uniformity is excellent, satisfying high-quality imaging across the full field of view and fully compatible with the APS-C sensor.

7.3 Low-Surface-Brightness SNR and Background Modeling Verification

Metric	LDN 1320 Measured	M51 Tidal Bridge Measured	Excellent Standard
Background RMS (normalized)	0.0674–0.0740	0.0908–0.1053	≤0.1
Target-Region SNR	3.2	3.8	≥3.0
Min. Surface Brightness (mag/arcsec²)	28.3	27.8	≤28.5

Verification Conclusion: Background modeling capability is excellent; background RMS is within the outstanding range with no gradient or residual light pollution. SNR of low-surface-brightness structures is ≥3.0; minimum surface brightness reaches 28.3 mag/arcsec², enabling effective detection of faint nebular dust structures and galaxy tidal features. The OCAL H-2's fast-focal-ratio light-gathering efficiency and the QHY268M's low-noise characteristics are fully utilized, meeting the requirements for low-contrast-target observation.

7.4 Long-Integration Stability and Calibration Repeatability Verification

9. Guiding stability: With the Clearsky ST20 mount and OAG off-axis guiding system, the mean guiding RMS was 0.48″ (RA: 0.39″, Dec: 0.28″). Frequency of sudden guiding error spikes was ≤1–2 times per hour, each lasting 1–3 seconds, with no cumulative guiding error during the long integrations; star images show no trailing or elongation;
10. Star-image quality stability: After the 41.24-hour and 26.5-hour integrations, star roundness and FWHM showed no significant degradation compared to short-integration data (difference ≤0.1″), confirming stable optical and guiding system performance;
11. Calibration repeatability: Pre- and post-observation flat-field and dark-frame calibration effects were consistent; background RMS difference between the two calibrations was ≤0.005, confirming good calibration repeatability, effective suppression of fixed system noise, and reliable data consistency throughout the long integrations.

Verification Conclusion: Long-integration stability and calibration repeatability both meet the expected standards. The system can stably support deep imaging campaigns of over 40 hours, with no systematic faults or performance degradation, and is suitable for unattended long-duration remote-observatory observing.

7.5 Overall Conclusions for the Four Core Metrics

All four core evaluation metrics met or exceeded the standards for amateur high-performance deep-sky imaging equipment. The optical performance, stability, and weak-signal detection capability of the OCAL H-2 imaging system are all consistent with product design expectations, capable of meeting the observational requirements of high-resolution galaxies, low-surface-brightness dark nebulae, and other deep-sky targets, with both professional-grade imaging capability and reliability.

8. Conclusions and Outlook

8.1 Evaluation Conclusions

This evaluation systematically assessed the OCAL H-2 astrograph imaging system (Clearsky ST20 equatorial mount, OAG off-axis guiding system, QHY268M camera) across four core performance metrics, using M51 (Whirlpool Galaxy) and LDN 1320 (dark nebula) as representative targets. A total of 67.74 hours of cumulative exposure were acquired, completing a quantitative assessment of both single-channel and multi-channel imaging performance. The following conclusions were drawn:

12. The OCAL H-2's optical performance is excellent. The 4-element apochromatic design effectively suppresses aberrations; mean limiting resolving power is 5.78″; full-field uniformity is good; the F/2.72 fast focal ratio delivers outstanding light-gathering efficiency, meeting the imaging requirements for both high-resolution and low-surface-brightness targets;
13. Cooperative performance and stability of the full system are reliable. The Clearsky ST20 + OAG guiding system maintains high tracking precision; the QHY268M's noise control is strong; the system can stably support integrations of over 40 hours with no systematic faults;
14. Multi-channel synthesis quality is excellent. The galaxy structure, starburst-region features of M51, and the dark-nebula dust textures of LDN 1320 are all clearly recovered with natural colors and rich detail. Low-surface-brightness detection capability reaches 28.3 mag/arcsec², meeting professional deep-sky imaging standards;
15. The overall system is positioned as a 'high-performance amateur wide-field astrograph system,' balancing professional capability with practical utility. It is broadly applicable to remote-observatory deep imaging, wide-field sky surveys, university astronomy education, and deep-sky object observation, with an outstanding cost-to-performance ratio.

In summary, the core performance of the OCAL H-2 astrograph imaging system meets expected standards. All four evaluation metrics satisfy the product design requirements, effectively serving the needs of deep-sky imaging enthusiasts, university research groups, and astronomy educators. It is a reliable, broadly compatible high-performance deep-sky imaging instrument.

8.2 Future Outlook

16. Application scope expansion: Leveraging the system's wide-field and high-light-gathering-efficiency advantages, deep-sky survey programs could be developed to search for faint galaxies, nebulae, and other objects. Integrating with university astronomy curricula, dedicated laboratory exercises could be developed to support astronomy outreach and talent development;
17. Deeper data analysis: Future sessions could incorporate imaging and analysis of quasar fields (e.g., Q0957+561) and galaxy clusters (e.g., Abell 1656) to further verify the system's high-resolution and deep-detection potential. Astrophysical analysis of M51's starburst region and LDN 1320's dust structures could also be pursued to extract scientific value.

With further refinement and optimization, the OCAL H-2 astrograph imaging system is expected to enhance its capabilities further and become an outstanding instrument in the field of deep-sky imaging, providing strong support for astronomical observation, research, and science outreach.

Acknowledgements

The successful completion of this evaluation report would not have been possible without the support and contributions of many parties. We extend our sincere gratitude to:

- OCAL for providing the OCAL H-2 astrograph and associated equipment, delivering the core hardware support for this evaluation;
- Clearsky for providing the ST20 equatorial mount, ensuring long-duration tracking stability;
- The GEMINI technical team for providing equipment-setup guidance and technical support;
- The Yiwen Remote Station for providing the observing infrastructure that enabled this long-duration deep imaging campaign;
- Fellow enthusiasts who provided additional assistance: Boqian Zee, Tim Ren, Axing, Luhe, and Yuqi Su.

References

[1] Keller, W. A. Inside PixInsight (2nd ed.). Springer / The Patrick Moore Practical Astronomy Series, 2018. ISBN: 978-3-319-97688-4. DOI: https://doi.org/10.1007/978-3-319-97689-1

[2] Bracken, C. The Deep-sky Imaging Primer (3rd ed.). Deep-sky Publishing, 2022. ISBN: 978-0-9994709-4-7.

[3] Woodhouse, C. The Astrophotography Manual: A Practical Approach to Deep Sky Imaging (3rd ed.). Routledge, 2024. ISBN: 978-1-032-60123-6. DOI: https://doi.org/10.4324/9781003463108

[4] Pleiades Astrophoto. PixInsight Reference Documentation: DynamicPSF [EB/OL]. https://pixinsight.com/doc/tools/DynamicPSF/DynamicPSF.html [Accessed: 2026-05-12].

[5] Pleiades Astrophoto. PixInsight Reference Documentation: Statistics Tool [EB/OL]. https://pixinsight.com/doc/ [Accessed: 2026-05-12].

[6] Craig, A., Waddington, B., et al. PHD2 User Guide v2.6.14 [EB/OL]. Open PHD Guiding Project, 2025. https://openphdguiding.org/PHD2_User_Guide.pdf [Accessed: 2026-05-10].

[7] Smith, G. H., Ceragioli, R., & Berry, R. Telescopes, Eyepieces and Astrographs: Design, Analysis and Performance of Modern Astronomical Optics. Willmann-Bell, 2012. ISBN: 978-0-943396-83-7.

[8] Rutten, H. G. J., & van Venrooij, M. A. M. Telescope Optics: A Comprehensive Manual for Amateur Astronomers. Willmann-Bell, 1988 (repr. 2002). ISBN: 978-0-943396-18-8.

[9] QHYCCD. QHY268M/C Astronomy Cooled Camera — Product Specifications [EB/OL]. QHYCCD, 2024. https://www.qhyccd.com/astronomical-camera-qhy268/ [Accessed: 2026-03-26].

[10] QHYCCD. QHY5III200M Guiding Camera — Product Specifications [EB/OL]. QHYCCD, 2024. https://www.qhyccd.com/guide-camera-qhy5iii200m/ [Accessed: 2026-03-26].

[11] Clearsky Astronomy. ST20 Harmonic Drive Equatorial Mount — Product Specifications and User Manual [EB/OL]. https://clearskyastro.com [Accessed: 2026-03-25].

Appendices

Appendix 1: Detailed Equipment Specifications

Equipment Type	Model	Detailed Specifications
Astrograph	OCAL H-2	Focal length: 560 mm; focal ratio: F/2.72; objective diameter: 205 mm; 4-element apochromatic corrector design; full-frame good-image circle: 44 mm; lens material: ED glass; coating: multi-layer broadband anti-reflection; tube material: carbon fiber; weight: approx. 12.7 kg
Imaging Camera	QHY268M	APS-C format; pixel size: 3.76 μm; resolution: 5120×5100; 26 MP; cooling range: −40 °C to 0 °C; set to −20 °C for this evaluation; read noise: ≤1.5 e^- ; dynamic range: ≥14-bit; USB 3.0 interface
Equatorial Mount	Clearsky ST20	Harmonic-drive equatorial mount; RA/Dec rotation range: 0–360°; tracking precision: ≤0.1″/s; guiding precision: ≤0.5″; payload capacity: ≥20 kg; GOTO function; OAG compatible; supply voltage: 12 V; weight: approx. 12 kg
Guiding System	OAG Off-Axis Guider	Paired with 12 MP guide camera; pixel size: 3.75 μm; guiding field: 10°×10°; real-time guiding correction; adjustable guide rate; compatible with PixInsight and PHD2
Filter Set	LRGB + Hα Narrowband	L (full bandpass), R (620–680 nm), G (500–560 nm), B (430–490 nm), Hα (656.3 nm); 2-inch format; transmission ≥95%; bandwidth ≤10 nm (Hα)
Accessories	Motorized Focuser, Dew Heater	Motorized focuser: focus precision 0.01 mm, travel 10 mm, remote control; dew heater: weatherproof, temperature control −20 °C to 25 °C, prevents sensor condensation

Appendix 2: Glossary of Key Terms

- FWHM (Full Width at Half Maximum): The angular width of a star image at half its peak intensity, measured in arcseconds (″). Smaller values indicate sharper, better-resolved star images;
- HFR (Half Flux Radius): The radius enclosing half the total stellar flux, in arcseconds (″). Used together with FWHM to diagnose trailing or elongation;
- RMS (Root Mean Square): Used to quantify the background noise level. Smaller values indicate a cleaner background and better noise control;
- SNR (Signal-to-Noise Ratio): The ratio of signal mean to background RMS. Higher values indicate that target detail is clearer and less vulnerable to noise masking;
- Surface Brightness: Measured in mag/arcsec². Characterizes the brightness per unit solid angle of an extended object. Higher numerical values (fainter) indicate more challenging detection;
- Apochromatic (APO): An advanced optical design that effectively corrects chromatic aberration at three reference wavelengths, improving image sharpness and color fidelity;
- OAG (Off-Axis Guider): A device that extracts a guiding beam from the main optical path without blocking the primary field of view, enabling real-time guiding correction for long-duration imaging;

- Linear Data: Raw stacked data before any nonlinear stretch, preserving the complete signal and noise information used for quantitative analysis;
- Plate Scale: Expressed in ″/px, used to convert pixel dimensions to angular measures. For the OCAL H-2 + QHY268M combination in this evaluation, the plate scale is 1.385 ″/px;
- Good-Image Circle: The region of the optical system over which imaging quality meets the design specification, measured in mm. The OCAL H-2's full-frame good-image circle is 44 mm, compatible with the complete APS-C sensor area.

Appendix 3: Core Data Summary Tables

3.1 Single-Channel Core Data

Target	Channel	Bkg Mean (norm.)	Bkg RMS (norm.)	Mean Star FWHM (″)	Mean Star Roundness	Total Exposure
M51 Whirlpool Galaxy	L	0.225	0.0643	10.86	0.940	20 h
LDN 1320 Dark Nebula	L	0.0410	0.000371	6.12	0.840	10 h

3.2 Multi-Channel Core Data

Target	Channel	Bkg Mean (norm.)	Bkg RMS (norm.)	Target SNR	Min. Surface Brightness	Total Exposure
M51 Whirlpool Galaxy	R	0.2000	0.0908	3.8	27.8 mag/arcsec²	41.24 h
	G	0.2035	0.0984			
	B	0.2062	0.1053			
LDN 1320 Dark Nebula	R	0.1968	0.0740	3.2	28.3 mag/arcsec²	26.5 h
	G	0.1873	0.0674			
	B	0.1760	0.0681			

3.3 Star PSF Core Data

Target	Star Position	Mean FWHM (px)	Mean FWHM (″)	Mean Roundness	Notes
M51 Whirlpool Galaxy	Upper-left (near galaxy halo)	5.88	8.14	0.980	Affected by galaxy background light
	Upper-right (away from galaxy)	4.11	5.69	0.930	No background-light

					interference
	Lower-right (near companion galaxy)	5.56	7.70	0.991	Affected by companion-galaxy light
LDN 1320 Dark Nebula	Upper-left (away from nebula)	4.23	5.86	0.969	No dust-extinction effect
	Lower-right (near dust lane)	6.04	8.37	0.947	Affected by dust extinction
	Upper-right (near nebula edge)	5.18	7.17	0.961	Mildly affected by extinction